The DOI for this manuscript is doi: 10.1175/JCLI-D-11-00512.1

The final published version of this manuscript will replace the preliminary version at the above DOI once it is available.

If you would like to cite this EOR in a separate work, please use the following full citation:

Chu, J., S. N.Hameed, and K. Ha, 2012: Non-linear, intraseasonal phases of the East Asian summer monsoon: Extraction and analysis using self-organizing maps. J. Climate. doi:10.1175/JCLI-D-11-00512.1, in press.

Article:

Non-linear, intraseasonal phases of the East Asian summer monsoon: Extraction and analysis using self-organizing maps

Jung-Eun Chu[1], Saji N. Hameed[2], and Kyung-Ja Ha[1]

[1]Division of Earth Environmental System, Pusan National University, Busan, Korea

[2]Center for Advanced Information Science and Technology, University of Aizu, Japan

8 September 2011

Submitted to Journal of Climate

03 April 2012 Revised

Corresponding Author

Prof. Kyung-Ja Ha

E-mail : kjha@pusan.ac.kr

Address: Division of Earth Environmental System, Pusan National University, Geumjeong-Gu, Busan 609-735, Korea

Abstract

We advance the hypothesis that regional characteristics of the East Asian summer monsoon (EASM) result from the presence of non-linear coupled features that modulate the seasonal circulation and rainfall at the intraseasonal timescale. To examine this hypothesis, we undertake the analysis of daily EASM variability using a non-linear multivariate data classifying algorithm known as self-organizing mapping (SOM).

On the basis of various SOM node analyses, we identify four major intraseasonal phases of the EASM. The first node describes a circulation state corresponding to weak tropical and subtropical pressure systems, weakened monsoonal winds, and cyclonic upper level vorticity. This mode, related to large rainfall anomalies in southeast China and southern Japan, is identified as the Meiyu–Baiu phase. The second node represents a distinct circulation state corresponding to a strengthened subtropical high, monsoonal winds and anticyclonic upper-level vorticity in southeast Korea, which is identified as the Changma phase. The third node is related to copious rain over Korea following Changma, which we name the post-Changma phase. The fourth node is situated diagonally opposite the Changma mode. Because Korea experiences a dry-spell associated with this SOM node, we refer to it as the dry-spell phase.

We further demonstrate that a strong modulation of the Changma and dry-spell phases on interannual timescales occurs during El Niño and La Niña years. Our results imply that the key to predictability of the EASM on interannual timescales may lie with analysis and exploitation of its non-linear characteristics.

1. Introduction

The East Asian summer monsoon (EASM) is well known for its intraseasonal and interannual variability. The rainy season known as Meiyu in China, Baiu in Japan, and Changma in Korea manifests regional differences that are prominent on the intraseasonal time-scale. The primary monsoon rainband associated with Meiyu and Baiu develops in mid-June in the lower regions of the Yangtze River Valley and in southern Japan, respectively (Kang et al. 1999; Wang et al. 2007). Conversely, the Korean rainy season involves two separate rainy periods: a main surge in mid-June, known as the Changma period, and a secondary surge in mid-August to early September, known as the post-Changma period (Kim et al. 2010; Wang et al. 2007). The modulation of regional rainy seasons of the EASM including Meiyu, Baiu, and Changma are regarded as meridional shifts of heavy rain belt, which may be a local manifestation of northward propagating climatological intraseasonal oscillation (CISO) (Wang and Xu 1997). Although the CISO displays regular phases change with respect to the calendar year, the northward propagations of summer monsoon ISO are not always phase locked (Wang and Rui 1990), so that the structure and propagation of the summer monsoon ISO tend to be more irregular (Yoo et al. 2010). Understanding the regional nature of EASM, particularly the underlying non-linear characteristics, may provide important insight to the difficulties in the seasonal to interannual predictability of EASM precipitation (Kang et al. 2002; Kim et al. 2008; Lee et al. 2011).

Most previous studies have examined intraseasonal variations embedded in the EASM by using statistical methods such as covariance analysis (Kang et al. 1999; Lau and Chan 1986) and multichannel singular spectrum analysis (Krishnamurthy and Shukla 2007). However, these linear analyses are limited in their ability to describe the full set of characteristics of monsoon subseasonal variation (Yoo et al. 2010). Thus, non-linear analysis has recently gained popularity.

Yoo et al. (2010) examined the spatial patterns of discrete rainfall states of the Asian summer monsoon intraseasonal phases derived from a hidden Markov model (HMM). However, a lack of explicit constraints to control the time scale of intraseasonal phases causes the HMM to simulate more high-frequency variability than that is actually observed (Jones 2009; Yoo et al. 2010). Chattopadhyay et al. (2008) adopted a self-organizing map (SOM) to objectively identify and explore non-linear characteristics of the Indian monsoon intraseasonal oscillation (ISO). Both of the above studies have focused on the near tropical ISO. A similar examination of the ISO within the more subtropical belt of the EASM domain was attempted by Chu and Ha (2011), but they only focused on methodological approach for monsoon intraseasonal phases. However, a dynamical analysis and interpretation of intraseasonal phases was not undertaken.

In this paper, we adopt the SOM methodology, a type of unsupervised, artificial neural network, to objectively identify non-linear phases embedded within the EASM circulation. In addition, we explore associated circulation states, teleconnections, and their manifestations on Korean rainfall. The main advantage of the SOM approach is that it provides a concise description of the main patterns of variability while accommodating non-linearity in the data. Further, it provides a powerful visualization of the underlying data structure and relations among the main modes of variability. A SOM analysis, together with a set of generalized patterns produced from the input data, describes the multidimensional distribution function of the data (Hewiston and Crane 2002; Kohonen 1990). The input data is a series of circulation state vectors composed of six important daily indices representing subtropical high-pressure regions, lower- and upper-level wind vectors, and vertical and horizontal wind shear. Our SOM analysis yields a non-linear classification of the continuum of atmospheric state vectors while preserving both the underlying probability distribution function of the data and the topological relationship between the states.

Scale interactions between interannual and intraseasonal modes of variability are aspects of EASM variability that carry important implications for predictability. In their study of the relationship between El Niño Southern Oscillation (ENSO) and ISO, Tam and Lau (2005) examined the propagation and growth/decay characteristics of ISO in various phases of ENSO on the basis of a lag correlation technique. Yun et al. (2009) discovered a significant lag correlation between interannual variability of northward propagating ISO, which has a quasi-biennial time-scale through preceding and concurrent summers, and ENSO events. Teng and Wang (2003) demonstrated that ENSO affects the northwestward-propagating ISO mode in the western North Pacific by changing the mean circulation through the vertical wind shear mechanism. Moreover, Yoo et al. (2010) showed the interannual modulation of the ISO associated with ENSO by employing a non-homogeneous HMM. Hence, an additional aspect of this study examines the relationship between the non-linear circulation states identified in our study and interannual climate modes, particularly ENSO.

The rest of the paper is organized in the following manner: In section 2 we describe the data and briefly explain the main ideas behind SOM methodology. In section3 we identify the intraseasonal phases and present underlying circulation patterns derived from SOM. Section 4 examines the relationship between intraseasonal phases and ENSO and Section 5 contains a summary and conclusions.

2. Data and methods

2.1 Observational datasets

The data used for the analysis of summer monsoon rainfall were collected from 1997 to 2008 by the daily Global Precipitation Climatology Project (GPCP). Because the daily GPCP began in October 1996, no earlier data was available. Data used for the analysis of large-scale circulation characteristics, including the geopotential height and horizontal components of winds at selected pressure levels, were collected from 1979 to 2008 by the National Centers for Environmental Prediction-National Center for Atmospheric Research (NCEP-NCAR) reanalysis (Kalnay et al. 1996). In addition, daily precipitation data collected at 79 synoptic stations located throughout the Korean Peninsula were used to examine regional rainfall amount.

2.2 East Asian summer monsoon indices

The EASM sometimes restricted to the subtropical monsoon that prevails over eastern China north of 20°N, Korea, Japan and adjacent marginal seas (Chen et al. 2000; Mao and Wu 2006). However, the EASM domain in this paper covers a large area from tropical regions including part of the western North Pacific to extratropical regions in order to include the western North Pacific subtropical high (WNPSH). The WNPSH is an important component in coupled circulation-convection system of EASM with its role of moisture transport and linkage between ENSO and EASM.

The evolution of the regional summer monsoon rainfall is accompanied and characterized by large-scale changes in the western North Pacific subtropical high (WNPSH), low-level winds and the associated moisture transport from the Indo-Pacific warm pool, upper-level Asian jet, vertical shear, and planetary-scale teleconnection patterns of circulation, among other features (Ha et al., 2005; Ha and Lee, 2007). Because of the similarity between the seasonal mean and dominant ISO mode (Ha et al., 2005), large-scale circulation indices can be used for the indices of the dominant intraseasonal mode. On the basis of dynamical consistency and regional relevance of precipitation intraseasonal phases, we chose six daily monsoon indices derived from circulation fields, excluding moisture fields (Table 1). The daily standardized anomalies of these six indices were constructed by subtracting the climatological daily mean.

i) The CI500H index represents a stationary anticyclone over the western North Pacific (Ha et al., 2005).

ii) The CI850U and CI850V indices represent low-level jets from the southwest flow over the Asian monsoon associated with a strong Changma. Advection of moist and warm air by low-level winds is essential for generating convective instability and sustaining convective activity (Ninomiya, 1980).

iii) The RM2 index, proposed by Lau et al. (2000), represents upper-level vorticity, a prominent feature of which is the northward advance of the western North Pacific subtropical high, which causes the axis of the climatological subtropical jet to migrate northward by about 10°–15° in latitude. Lau et al. (2000) argued that this process represents a remarkable response of the subtropical upper-level flow to tropical heating in the Southeast Asian region.

iv) The SI index represents the vertical shear index, as described in Wang et al. (1998). The vertical shear of zonal wind represents the zonal thermal winds between 850 and 200 hPa that result from north–south and land–sea thermal contrasts.

v) The western North Pacific monsoon index (WNPMI) represents the difference of 850 hPa westerlies between a southern region (5°N–15°N, 110°E–130°E) and a northern region (20°N–30°N, 110°E–140°E). This latitudinal differential westerly index reflects not only the strength of the tropical westerlies but also the intensity of the low-level vorticity associated with the Rossby wave response to the Philippine Sea convective heat source (Wang et al., 2001).

2.3 Self-organizing map

a. The SOM algorithm

The SOM consists of two layers: input and competitive. The input layer is fully connected to the competitive layer of map nodes (Fig. 1). When an input is presented, the output nodes compete to represent the pattern. The SOM's two processes are that of training and mapping. The key to the ability of the SOM to extract patterns is the way that it learns; this is embodied in its training algorithm. Artificial neural networks learn by an iterative process, whereby input data are presented successively to the networks. The initial step in this iterative procedure is to randomly distribute nodes in the data space. Thus, in our two-dimensional example, nodes were initially a random cloud of points in two dimensions. After successive presentation of the input data to the network, the nodes approach the positions that best represent the input data. The number of nodes (output patterns) is defined by the user and is dependent upon the level of detail desired in the analysis. In our study, we applied 3 × 3 nodes physically considering active, break, and normal basic states and their underlying substates of ensemble mean, above state, and below state (Chattopadhyay et al., 2008). The reason why we have used 3×3 SOM map is that the 3×3 map is most effectively distinguish the four intraseasonal phases. To ensure the robustness of the SOM analysis, we examined the sensitivity of SOM map sizes (Figure not shown). Since SOM classification include both major and subsequent modes, small number of nodes may superimpose the transitional properties of intraseasonal phases on the major modes. To include both major and subsequent modes together, larger number of nodes than that of major nodes should be needed. If SOM have larger than 3×3 map, however, the major modes are not clearly distinguished to adjacent modes (Figure not shown). Mathematically, the principal goal choosing the number of clustering is to maximize similarity within clusters and minimize similarity between clusters. Therefore, based on consideration of mathematical optimization and the physical requirement of identifying distinct patterns, a configuration of 3 × 3 states is chosen.

The general SOM training algorithm is outlined below; mathematical details can be found elsewhere (Kohonen, 1997). All input vectors are fully connected to nodes in the competitive layer, and the nodes are uniquely defined by a reference vector consisting of weighting coefficients. Adjustment of the reference vectors to the input vector, an essential part of SOM, is achieved through a user-defined iterative cycle. This adaptation minimizes the Euclidean distance (EUD) between the reference vector for any jth node W_j and the input data vector X, that is to find:

$$\mathrm{EUD} = \left|X - W_j\right| = \sqrt{\sum_{i=1}^{n}(X_i - W_{ij})^2}$$

The first input sample is then compared with each node in the competitive layer. The node with the least Euclidean distance between itself and the input vector is known as the winning node. During the iterative process, the winner node updates the reference vector and its associated weights together with those of neighbor nodes within the neighborhood radius. Since each node has to be adjusted relative to its neighbor, inclusion of the neighborhood makes the SOM classification nonlinear. The training cycle may be continued n times, and updating equations are described as

$$W_j(n+1) = \begin{cases} W_j(n) + c(n)\left[\mathrm{X}(n) - W_j(n)\right], & j \in R_j(n) \\ W_j(n), & otherwise \end{cases}$$

In this reference vector for the jth node for nth training cycle, $X(n)$ is the input vector; $R_j(n)$ is the predefined neighborhood around node j; and $c(n)$ is the neighborhood kernel, which defines the neighborhood. The neighborhood kernel may be a monotonic decreasing function of n ($0 < c(n) < 1$, known as a bubble, or it may be of Gaussian type as

$$\alpha(\mathrm{n})\exp\left[\frac{-\left\|r_j - r_i\right\|^2}{2\sigma^2(n)}\right]$$

where $\alpha(\mathrm{n})$ and $\sigma(n)$ are constants monotonically decreasing with n. Here, $\alpha(\mathrm{n})$ is the learning rate, which determines the velocity of the learning process, while $\sigma(n)$ is the amplitude, which determines the width of the neighborhood kernel. We used Gaussian type as the neighborhood kernel. In addition, r_j and r_i are the coordinates of the nodes j and i, respectively, in which the neighborhood kernel is defined. Throughout training, the learning rate and size of the update neighborhood—the update radius—decrease, leading to progressively refined initial generalized patterns. Finally, the SOM consists of a number of patterns characteristic of the data, with similar patterns nearby and dissimilar patterns farther apart. After the training process, the final map, or reference vector, is completed. The mapping process distributes each input vector to a corresponding reference vector based on its similarity, such as the least Euclidean distance. In this way, the nodes in a self-organizing map compete to most effectively represent the particular input sample.

b. Implementation of SOM

An input vector contains six components of circulation indices for a particular day (Fig. 1). Similarly, the corresponding reference vector has six weighting coefficients. Once we obtained classifications using the SOM algorithm, the dates from June to August (JJA) over 30 years from 1979 to 2008 were collected at each node. Thus, the number of input samples was 2760, representing 30 years × 92 days JJA, which were finally mapped onto a two-dimensional (3 × 3) lattice. Each node contains a reference vector consisting of six indices and clustered dates. The composite of classified dates provided a spatial structure of each phase. That is, if the summer monsoon ISO is a convectively coupled oscillation, each pattern should be strongly related to a particular phase of the precipitation oscillation. In addition to spatial pattern, the clustered dates add temporal information.

3. Results

3.1 Identification of intraseasonal phases derived from SOM

A composite of classified dates was performed in section 3.2 to detect the geographical rainfall structure of each node. To include information of basic statistics of intraseasonal phases, we showed the mean days per event, percent frequency of days, and probability of no transition at each node (Table 2). Here, the number of events was determined by counting the total number of times the data records were mapped consecutively to a particular node with no break. Mean days per event were defined by averaging the number of consecutively mapped days per event. Frequency of days was defined as the number of days clustered in a particular node divided by the total number of days used in the classification (30 year × 92 days/year). The probability of no transition, also expressed in percentage, is the probability that, when an input vector corresponding to a particular day is mapped to a node, the next day will be mapped again to the same node. Thus, for the (1,1) node, 78.9% of the cases are successively projected onto the node. Similarly, it is of the same order for the node (3,3) and is lowest for (2,2). This implies that, when a day is attached to a (1,1) or (3,3) node, the next day shows the highest probability of clustering at the same node; the chance is lowest for the node (2,2). Further, it can be seen that mean days per event is highest for the (1,1) node with 6 days and (3,3) node with 5 days and the corresponding percentages of frequencies of days clustered at these nodes are also higher. Comparing to results based on Indian summer monsoon suggested by Chattopadhyay et al. (2008), there are four nodes that are sustainable and have greater portion while two major nodes are found for Indian monsoon ISO.

The statistics described above can be used to examine the typical timescales of variability for any chosen node. It is well known that the intraseasonal oscillation of EASM has a broadband spectrum ranging from 20 to 60 days. It has been proposed that northward propagating oscillation exhibits dominant periodicities in the 30-60-day (Tsou et al. 2005; Wang and Xu 1997, Yun et al. 2009) or 20-50-day (Mao et al. 2010) timescales over the North Pacific and East Asian region. Another periodicity of 10-20-day oscillation controls the behavior of the SCS summer monsoon and Yangtze rainfall for most of years (Chen and Chen 1995; Mao and Chan 2005). This broadband nature of the frequency spectrum may be due to non-linear interaction between the dominant periodicities and higher and lower periodicities. In comparison with ISO periodicities mostly derived by filtered OLR or precipitation anomalies, we present the periodicity of an ISO event using a persistence of each intraseasonal phase from discretized dates obtained through SOM analysis. The persistence is represented as a mean days per event in Table 2. Assuming that one full cycle of intraseasonal phase is an episode, the total number of days per episode is 33, which corresponds to the most dominant periodicity of an ISO over the East Asian region. Thus, the above results demonstrate the quantitative estimate of the ISO within a season available in various sources and allows for further application of the SOM to study the monsoon ISO.

On the basis of intraseasonal phases derived from the SOM algorithm, the spatial patterns of four nodes including (1,1), (3,1), (3,3) and (1,3) were considered as major modes; their underlying dynamical fields are suggested in section 3.3.

3.2 Classification of precipitation states

The composite precipitation corresponding to the clustered dates of four major nodes are shown in Fig. 2 (full figures of nine nodes can be found in Chu and Ha (2011)). In (1,1), the zonally elongated rainfall in southeast China and southern Japan is similar to onset structure called as Meiyu and Baiu. Following a counter-clockwise direction, the (2,1) node shows a northward shifted center of rainfall over southern Korea and southeastern Japan (figure not shown). The (3,1) and (3,3) nodes represent Changma-like pattern with copious rainfalls over Korea. The observed data from Korean synoptic stations also demonstrate that the rainfall averages in the nodes are almost three-times higher than those in opposite nodes (not shown). While the regions over 25°N show similar patterns, distinct differences among Changma-proper nodes can be found over the subtropical western Pacific regions. Dry conditions appear along the western North Pacific high in the (3,1) node, and wet conditions dominate over the subtropical western North Pacific in the (3,3) node. Temporal analysis shows that the (3,3) phase occurs following the Changma season rains. It is interesting to note that SOM distinguishes the secondary peak of Korean rain, which has been recently regarded as the post-Changma season. In the (1,3) node, continental regions experience a dry spell associated with the condition, while oceanic areas have scattered rainfall distribution. The northward propagation of the convective center can be seen by following the panels counter-clockwise starting from (1,1) in Fig. 2.

Until now, we have found that SOM effectively captured the regional characteristics of various phases in intraseasonal monsoon precipitation. However, this method does not clearly explain the temporal evolution between different intraseasonal phases. Figure 3 shows the number of clustered days in JJA for 30-year periods in four major nodes so that the seasonal variation can be seen (full figures of nine nodes can be found in Chu and Ha (2011)). For example, if each case of 1 June is clustered in the (1,1) node from the entire 30-years periods, it will be shown as 30 for 1 June. It is evident that the early stage of summer tends to be clustered at the (1,1) node, and the maximum days for each cluster shows the movement along the counter-clockwise direction starting from the (1,1) node. According to Fig. 3(b), many portion of days for (3,1) node are concentrated at mid-June to late-July; this period is equivalent to the Changma season. The maximum number of clustered days in (1,1) node and (3,1) node are June 1 and July 4, respectively. In the (3,3) node, days appeared in late June and gradually increased in early August. August is regarded as the prime season for tropical cyclones such as typhoons. Many days for August are divided into (3,3) and (1,3) nodes. Although the number of days of (2,1) and (2,3) nodes are evenly distributed throughout the summer, not much variance is evident (figure not shown). It can be found that there is specific preference for each node during the summer season and oscillating feature of the nodes. This result also indicates that each mode can be viewed as one components of monsoon ISO that are phase-locked to the seasonal cycle to a certain degree.

On the basis of the precipitation patterns and evolutionary history of nine nodes, four major nodes, (1,1), (3,1), (3,3) and (1,3), were named Meiyu-Baiu, Changma mode, post-Changma, and dry-spell modes, respectively. In addition, we performed empirical orthogonal function (EOF) analysis (Fig. 4). It was found that EOF1 resembles the Meiyu-Baiu mode, while

EOF2 is similar to the Changma mode on the basis of pattern correlation coefficients of 0.65 and 0.30, respectively. However, the post-Changma and dry-spell modes are not shown in EOF analysis, which indicates that SOM can capture the distinguished patterns between Changma and post-Changma modes and the terminated monsoon precipitation structure in the dry-spell mode. It is clear that the SOM technique, through the use of many large-scale circulation parameters, is able to capture the low-frequency subseasonal variability of rainfall over East Asia. In this study, we use six large-scale monsoon indices including CI500H, CI850U, CI850V, RM2, SI and WNPMI selected as predictors. To ensure the robustness of the SOM analysis, we examined the sensitivity of predictors to SOM classification by removing each index from others. The results exhibit that almost identical patterns of four major modes can be captured even though one predictor is removed (Figure not shown). Most of the pattern correlation coefficients (PCCs) between four major modes from original experiment and those from sensitivity experiments show higher than 0.9 values. However, dry-spell mode is rather sensitive to CI500H with its relatively lower PCC 0.69. Considering that PCC 0.69 is still substantial value, the set of six large-scale indices can be reasonable predictors. The patterns of dynamical field and interpretation associated with each mode are subsequently discussed in detail.

3.3 Large-scale circulation related to intraseasonal phases

The large-scale patterns of several other dynamical variables associated with the four major modes identified by the SOM techniques are noted in Fig. 5. 200 hPa zonal wind and 850 hPa wind anomalies are presented to observe the extension of upper-level jet stream and low level moisture transport, respectively. Rossby wave propagation is described by 500 hPa geopotential height. Based on an analysis of the various SOM nodes, we identified four major intraseasonal phases of the EASM located at the far corners of the SOM. These four nodes correspond to two major circulation patterns with opposite phases.

In the Meiyu-Baiu mode, a zonally elongated jet stream is conspicuous, which represents a circulation state corresponding to weak tropical and subtropical pressure systems over the western Pacific, weakened monsoonal winds, and cyclonic upper-level vorticity over the Asian jet exit region. However, the vertical wind shear is large with stronger westerly winds in the upper troposphere (Fig. 5). This effect is also linked to relatively warmer conditions over the Indian Ocean produced by a heat-induced high and cooler condition over the Asian continents (figure not shown). This meridional temperature gradient can reinforce the jet stream through a thermal wind relationship.

The Changma mode occurs with a distinct circulation state corresponding to a strengthened subtropical high, monsoonal winds and anticyclonic upper-level vorticity to southeast Korea. However, the vertical shear is weak with a weaker upper-level westerly associated with a weaker and northward shifted subtropical jet stream. Advection of moist, warm air by low-level winds is essential for generating convective instability and sustaining convective activity (Ninomiya 1980; Ha et al. 2005). The cold, dry inflow produced by cyclonic circulation between western Pacific high (WPH) and the Okhotsk High and warm and moist air produced by WPH demonstrate the convective instability that provides reasonable intense precipitation over the Korean Peninsula. The upper- and lower-level circulation features of the Changma mode correspond to the strong Changma patterns discussed by Ha et al. (2005). Another interesting feature is the presence of a weakened tropical high-pressure system extending from the South China Sea to the Philippines.

A mirror image of the node representing the Meiyu–Baiu phase can be observed in the circulation vector at its diagonally opposite corner (refer to Fig. 3 in Chu and Ha (2011)). Temporal analysis shows that this phase occurs after the Changma season rains and the mid-summer dry period. Copious rains occur over Korea during this period, known as the post-Changma phase. The prominent circulating feature of the mode is the northeastward advance of WPH and convective activity over the subtropical western Pacific. The main effect of the northward advance of the western North Pacific subtropical high causes the axis of the climatological subtropical jet to migrate northward by about 10°–15° in latitude (Lau et al., 2000), which represents a remarkable response of the subtropical upper-level flow to tropical heating over the western Pacific. A wave train pattern can be found from the Philippine Sea to the west coast of North America, which is considered as convectively coupled Rossby wave-like system triggered by anomalous convective activity over the tropical western North Pacific (Hsu and Weng 2001; Mao et al. 2010).

The dry-spell mode is also diagonally opposite the Changma mode and features a mirror image of the circulation vector. A low-pressure anomaly develops over the subtropical western Pacific while a high-pressure anomaly intensifies northeast of the low-pressure anomaly. The southwestward transport of moisture from the Pacific Ocean increases precipitation near the South China Sea. This process also terminates moisture transport from the equatorial Pacific into East Asia, which in turn creates dry conditions in Korea.

4. Relationship between ENSO and intraseasonal phases

4.1 Lead-lag correlations between ENSO events and intraseasonal phases

On the interannual time scale, the intraseasonal phases can be affected by slowly varying ‘external’ components such as ENSO. The interannual relationship between ENSO and intraseasonal phases will help to overcome uncertainty in the prediction of interannual variability (IAV). Various studies have been performed on the lead-lag relationship between the tropical pacific SST and the East Asian monsoon system (Chang et al. 2000; Lau and Weng 2001; Wu et al. 2003; Lau and Wang 2006; Lee et al 2005; Wang et al. 2000). Typically, it has been considered that rainfall of EASM tends to be enhanced following the preceding El Niño, which has a mature phase during the boreal winter December through February (DJF). El Niño persistently influences circulation and rainfall anomalies in East Asian through the following summer JJA. However, the relationship between equatorial eastern Pacific SST anomalies and rainfall in East Asia remains a controversial issue. Chen et al. (1992) argued that significant correlations could not be detected between eastern Pacific SST anomalies and EASM. These diverse results imply that interannual variation of the EASM is probably influenced by complex air-sea-land and tropical-extratropical interactions (Wang et al. 2000).

The ENSO teleconnection is broadly characterized by anomalous Philippine Sea anticyclone results from a Rossby wave response to suppressed convective heating (Wang et al. 2000; Wu et al. 2003). To support our hypothesis that the intraseasonal phases of EASM are related with ENSO, we constructed composite difference diagram of simultaneous summertime (JJA) 850-hPa geopotential height anomalies and preceding wintertime SST (DJF) for years with high and low occurrences of the four modes (Fig. 6). To obtain the high and low occurrence year, we normalized the annual number of clustered days. If normalized annual number of days is exceed one standard deviation, the year is regarded as high occurrence year and is below minus one standard deviation, the year is regarded as low occurrence year.

As shown in Fig. 6, the high occurrence years for Meiyu-Baiu mode and Changma mode are significantly related with anomalous anticyclone over the western North Pacific (Fig. 6 (a) and (b)) while those for post-Changma mode and dry-spell mode are associated with cyclonic circulation (Fig. 6 (c) and (d)). Another interesting feature is the positive (negative) values over the central equatorial Pacific for Meiyu-Baiu mode and Changma mode (dry-spell mode). It implies that the intraseasonal phases are somewhat connected to tropics. The evidence of relationship between tropical SST and extratropical intraseasonal phases can also be found in Fig 6 (e) - (h). Although Meiyu-Baiu mode and post-Changma mode are not significantly correlated to thermal condition over the equatorial eastern Pacific during preceding winter, there is a distinct difference between four major modes. The high occurrence years for Meiyu-Baiu mode and Changma mode tend to be related with El Niño-like pattern over the equatorial eastern Pacific during preceding winter while those for post-Changma mode and dry-spell mode exhibit La Niña-like pattern. Thermal condition over the Kuroshio extension region is rather significant for Meiyu-Baiu mode. Similar patterns with opposite is identified in Changma mode and dry-spell mode. Significant positive (negative) SST can be found over equatorial central Indian Ocean and eastern Pacific for Changma mode (dry-spell mode).

The seasonal evolution of relationship between equatorial eastern Pacific SST and each intraseasonal phase of EASM is examined by lead-lag correlations of four major modes. The interannual variability of these modes—Meiyu–Baiu, Changma, post-Changma, and dry-spell—is depicted by using the annual number of clustered days. A time series of the seasonal mean Niño-3 index from a lead time of DJF to a lag time of July-September (JAS) was prepared to calculate the correlation coefficient (CC). Figure 7 shows the lead-lag CC between the Niño-3 index and the four major modes. The Meiyu-Baiu and Changma modes, which occur in early summer, positively correlate with the eastern Pacific SST for the preceding winter. This relationship is maintained until following spring but is not significant after March-May (MAM). For all lead-lag periods from DJF to JAS, the CC between the Niño-3 index and the Changma mode is twice than that of the Meiyu-Baiu. On the contrary, the post-Changma and dry-spell modes, which occur in later summer, show negative correlation with the proceeding winter-to-spring Niño-3 index. CCs for these modes start with a similar value as that in DJF and the same as that in February to April (FMA). Although an abrupt decline is shown in the dry-spell mode, however, the CC for the post-Changma mode is more persistent. The opposite lead-lag CCs among the four major modes indicate that particular monsoon phases are favorable to ENSO.

4.2 ENSO impacts on intraseasonal phases

In the previous sections, we demonstrated that particular monsoon phases are favored by preceding ENSO events. The reason why the response of four intraseasonal modes to ENSO is not linear is fundamentally due to the non-linear atmospheric response to warm and cold ENSO. The composite circulation fields or four major modes for the years with preceding wintertime El Niño and La Niña show asymmetric structure and it demonstrates the non-linear relationship between intraseasonal phases and ENSO.

Here, we quantitatively demonstrate the impact of preceding winter ENSO events on intraseasonal phases by using the mean annual number of days per events. For the representative ENSO events, we selected eight El Niño years including 1983, 1987, 1988, 1992, 1995, 1998, 2003, and 2007 and eleven La Niña years including 1984, 1985, 1986, 1989, 1996, 1997, 1999, 2000, 2001, 2006, and 2008. The definition of these ENSO years was based on a threshold of +/-

0.5 °C for the DJF Niño-3 index with a three-month running mean of SST anomalies in the Niño-3 region (5°N-5°S, 150°-90°W).

The mean number of days per event clustered during ENSO years for the four major modes is shown in Fig. 8. Of the 92 clustered days in one year, that in JJA was 16.9, 13.6, 16.7, and 11.6 for the Meiyu–Baiu, Changma, post-Changma, and dry-spell modes, respectively. It is interesting to note that the mean the number of days for El Niño events increased in the Meiyu–Baiu and Changma modes by 38% and 45%, respectively. On the contrary, these results decreased in post-Changma and dry-spell modes by 32% and 58%, respectively, which indicates that the Meiyu–Baiu and Changma modes are favored by the preceding winter El Niño. However, La Niña association appears to be different. No specific preference for the Meiyu–Baiu or post-Changma mode is indicated by a preceding La Niña event, although the Changma mode (dry-spell mode) tends to occur less (more) frequently through winter equatorial eastern SST cooling. Thus, indications on the modulation of variation by external components such as ENSO could aid prediction of nonlinear monsoon precipitation ISO over East Asia.

5. Summary and Conclusions

Nonlinear variability of monsoon rainfall creates difficulties in predicting the intraseasonal precipitation of EASM. We hypothesized that the summer monsoon intraseasonal phases are convectively coupled oscillation, and hence, it should be possible to identify the phases of rainfall oscillation by using large-scale circulation parameters. However, the relationship between rainfall and circulation is non-linear; therefore, an effective method for isolating the commonality among the parameters is necessary such that various phases of nonlinear convectively coupled intraseasonal oscillation are detected. For this reason, we adopted a non-linear pattern recognition algorithm known as SOM in this study. Unlike the linear techniques, SOM is capable of identifying the various intraseasonal phases of EASM, including their evolutionary histories. This advantage of SOM will provide extended-range prediction of intraseasonal monsoon precipitation.

We used six large-scale circulation indices to describe the intraseasonal phases of EASM (Table 1). The daily large-scale dynamical indices used as SOM algorithm input parameters demonstrate that it captures the temporal evolution and the spatial patterns associated with different intraseasonal phases of the monsoon rainfall (Fig. 2). This result proves the strength of the SOM technique in isolating out the non-linear coupled states and establishes that the monsoon intraseasonal phases are non-linear coupled oscillation. On the basis of an analysis of the various SOM nodes, we identified four major intraseasonal phases of the EASM, which were positioned at the far corners of the SOM. The first node described a circulation state corresponding to weak tropical and subtropical pressure systems, weakened monsoonal winds, and cyclonic upper-level vorticity. However, the vertical wind shear was large with stronger westerly winds in the upper troposphere. This mode, which is related to large rainfall anomalies in southeast China and southern Japan, occured several weeks prior to the onset of Changma rains in Korea. Based on its various characteristics, we identified this mode as the Meiyu-Baiu phase. The second node selected for this analysis represented Changma over Korea and occured with a distinct circulation state corresponding to a strengthened subtropical high, monsoonal winds, and anticyclonic upper-level vorticity in the southeast Korea. However, the vertical shear was weak with a weaker upper-level westerly associated with a weaker and northward-shifted subtropical jet stream. Another interesting feature is the presence of weakened tropical high pressure systems extending from the South China Sea into the Philippines. The third node is related with copious rains over Korea, which we termed the post-Changma phase. Temporal analysis showed that this phase occured after the Changma season rains and the mid-summer dry period. The fourth node was diagonally opposite to Changma mode and featured a mirror image of the circulation vector. Because Korea experienced a dry spell associated with this SOM node, we named it the dry-spell phase.

In addition, we considered the modulation of monsoon intraseasonal characteristics by external components such as ENSO to provide assistance in the prediction of monsoon precipitation over East Asia. We discovered that the Meiyu-Baiu mode and Changma mode are favored by the preceding winter El Niño. However, a different La Niña association was apparent. No specific preference for the Meiyu-Baiu mode or post-Changma mode was detected by the preceding La Niña event, although the Changma mode (dry-spell mode) tended to be less (more) frequent through winter equatorial eastern SST cooling. The results have great implications in improving the predictability of interannual variability, which is controlled by the non-linear and chaotic monsoon intraseasonal precipitation.

Acknowledgments

This work was supported by the National Research Foundation of Korea (NRF) grant funded by the Korea government (MEST) (No.2011-0021927, GRL).

REFERENCES

Chang, C.-P., Y. Zhang, and T. Li, 2000: Interannual and interdecadal variations of the East Asian summer monsoon and tropical Pacific SSTs. Part I: Roles of the subtropical ridge. *J. Climate*, **13**, 4310–4325.

Chattopadhyay, R., A. K. Sahai, and B. N. Goswami, 2008: Objective Identification of nonlinear convectively coupled phases of monsoon intraseasonal oscillation: Implications for prediction. *J. Atmos. Sci.*, **65**, 1549-1569.

Chen, L., M. Dong, and Y. Shao, 1992: The characteristics of interannual variation on the East Asian monsoon. *J. Meteor. Soc. Japan*, **70**, 397-421.

Chen, T.-C., and J.-M. Chen, 1995: An Observational Study of the South China Sea Monsoon during the 1979 Summer: Onset and Life Cycle. *Mon. Wea. Rev.*, **123**, 2295–2318.

Chen, T.-C., M. C. Yen, and S. P. Weng, 2000: Interaction between the summer monsoons of East Asia and South China Sea: Intraseasonal monsoon modes. *J. Atmos. Sci.*, **57**, 1373–1392.

Chu, J.-E., and K.-J. Ha, 2011: Classification of Intraseasonal Oscillation in Precipitation using Self-Organizing Map for the East Asian Summer Monsoon, *Atmosphere*, **21(3)**, 221-228.

Ha, K.-J., and S.-S. Lee, 2007 : On the interannual variability of the Bonin high associated with the East Asian summer monsoon rain. *Climate Dyn.*, **28(1)**, 67-83.

Ha, K.-J., S.-K. Park, and K.-Y. Kim, 2005: On interannual characteristics of climate prediction center merged analysis precipitation over the Korean peninsula during the summer monsoon season. *Int. J. Climatol.*, **25**, 99-116.

Hewitson, B. C., and R. G. Crane, 2002: Self-organizing maps: Applications to synoptic climatology. *Climate Res.*, **22**, 13-26.

Hsu, H.-H., and C.-H. Weng, 2001: Northwestward propagation of the intraseasonal oscillation in the western North Pacific during the boreal summer: structure and mechanism. *J. Climate*, **14**, 3834-3850.

Jones, C., 2009: A homogeneous stochastic model of the Madden–Julian oscillation. *J. Climate*, **22**, 3270–3288.

Kalnay, E., and Coauthors, 1996: The NCEP/NCAR 40-Year Reanalysis Project. *Bull. Amer. Meteor. Soc.*, **77**, 437-471.Kang, I.-S., and Coauthors, 2002: Intercomparison of the climatological variations of Asian summer monsoon precipitation simulated by 10 GCMs. *Climate Dyn.*, **19**, 383–395.

Kang, I.-S., C.-H. Ho, and Y.-K. Lim, 1999: Principal Modes of Climatological Seasonal and Intraseasonal Variations of the Asian Summer Monsoon. *Mon. Wea. Rev.*, **127**, 322-340.

Kim, H.-M., I.-S. Kang, B. Wang, and J.-Y. Lee, 2008: Interannual variations of the boreal summer intraseasonal variability predicted by ten atmosphere-ocean coupled models. *Climate Dyn*., **30**, 485–496.

Kim, K.-Y., J.-W. Roh, D.-K. Lee, and J.-G. Jhun, 2010: Physical mechanisms of the seasonal, subseasonal, and high-frequency variability in the seasonal cycle of summer precipitation in Korea, *J*. Geophys. Res., **115**, D14110.

Kohonen, T., 1990: The self-organizing map. *Proc. IEEE,* **78**, 1464-1480.

Kohonen, T., 1997: Self-organizing maps. *Springer series in information sciences, Springer-Verlag*, *Berlin ISBN 3-540-67921-9.*

Krishnamurthy,V., and J. Shukla, 2007: Intraseasonal and seasonally persisting patterns of Indian monsoon rainfall. *J. Climate*, **20,** 3-20.

Lau, K.-M., and H. Weng, 2001: Coherent modes of global SST and summer rainfall over China: An assessment of the regional impact of the 1997-98 El Niño. *J. Climate*, **14**, 1294-1308.

Lau, K.-M., and P. H. Chan, 1986: Aspects of the 40-50 day oscillation during the northern summer as inferred from outgoing longwave radiation. *Mon. Wea. Rev.*, **114**, 1354-1367.

Lau, K.-M., and S. Yang, 2000: Dynamical and boundary forcing characteristics of regional components of the Asian summer monsoon. *J. Climate*, **13**, 2461–2482.

Lau, N.-C., and B. Wang, 2006: Interactions between Asian monsoon and the El Niño-Southern Oscillation. The Asian Monsoon, B. Wang, Ed., *Springer/Praxis Publishing*, 478-552.

Lee, E.-J., J.-G. Jhun, and C.-K. Park, 2005: Remote connection of the northeast Asian summer rainfall variation revealed by a newly defined monsoon index. *J. Climate*, **18**, 4381-4393.

Lee, S.-S., J.-Y. Lee, K.-J. Ha, Bin Wang, and J. Schemm, 2011: Deficiencies and possibilities for long-lead coupled climate prediction of the Western North Pacific-East Asian summer monsoon, *Climate Dyn.*, **36**, 1173-1188.

Mao J., and J. C. L. Chan, 2005: Intraseasonal variability of the South China Sea summer monsoon. *J. Climate*, **18**, 2388–2402.

Mao, J. Y., and G. X. Wu, 2006: Intraseasonal variations of the Yangtze rainfall and its related atmospheric circulation features during the 1991 summer. *Climate Dyn.*, **27**, 815–830.

Mao, J., Z. Sun, and G. Wu, 2010: 20–50-day oscillation of summer Yangtze rainfall in response to intraseasonal variations in the subtropical high over the western North Pacific and South China Sea. *Climate Dyn.*, **34**, 747–761.

Ninomiya K., 1980: Enhancement of Asian subtropical front due to thermodynamic effect of cumulus convection. *J. Meteor. Soc. Japan,* **58**, 1-15.

Tam, C.-Y., and N.-C. Lau, 2005: Modulation of the Madden-Julian Oscillation by ENSO: Inferences from observations and GCM simulations. *J. Meteor. Soc. Japan*, **83**, 727-743.

Teng, H., and B. Wang, 2003: Interannual variations of the boreal summer intraseasonal oscillation in the Asian-Pacific region. *J. Climate*, **16**, 3572-3584.

Tsou, C.-H., P.-C. Hsu, W.-S. Kau, and H.-H. Hsu, 2005: Northward and northwestward propagation of 30–60 day oscillation in the tropical and extratropical western North Pacific. *J. Meteor. Soc. Japan*, **83**, 711–726.

Wang, B., and H. Rui, 1990: Synoptic climatology of transient tropical intraseasonal convection anomalies: 1975–1985. *Meteor. Atmos. Phys.*, **44**, 43-61.

Wang, B., and X. Xu, 1997: Northern Hemisphere Summer Monsoon singularities and Climatological Intraseasonal Oscillation. *J. Climate*, **10**, 1071-1085.

Wang, B., J.-G. Jhun, and B.-K. Moon, 2007: Variability and Singularity of Seoul, South Korea, Rainy Season (1778–2004). *J. Climate*, **20**, 2572–2580.

Wang, B., R. Wu, and K.-M. Lau, 2001: Interannual Variability of the Asian Summer Monsoon: Contrasts between the Indian and the Western North Pacific–East Asian Monsoons. *J. Climate*, **14**, 4073–4090.

Wang, B., R. Wu, and X. Fu, 2000: Pacific-East Asian teleconnection: How does ENSO affect East Asian climate? *J. Climate*, **13**, 1517-1536.

Wang, Q., Y. H. Ding, and Y. Jiang, 1998: Relationship between Asian monsoon activities and the precipitation over China mainland. *J. Appl. Meteor.*, **9**, 84-89.

Wu, R., Z.-Z. Hu, and B. P. Kirtman, 2003: Evolution of ENSO related rainfall anomalies in East Asia. *J. Climate*, **16**, 3742-3758.

Yoo, J.-H., A. W. Robertson, and I.-S. Kang, 2010: Analysis of Intraseasonal and Interannual Variability of the Asian Summer Monsoon Using a Hidden Markov Model. *J. Climate*, **23**, 5498–5516.

Yun, K.-S., B. Ren, K.-J. Ha, J. C. L. Chan, and J.-G. Jhun, 2009: The 30-60-day oscillation in the East Asian summer monsoon and its time-dependent association with the ENSO. *Tellus*, **61A**, 565–578.

Table Captions

Table 1. Description of the six East Asian summer monsoon circulation indices. U is zonal wind, Vis meridional wind, and Z is geopotential height.

Table 2. Mean days per event, represented by bold type. Percent frequency of days and the probability of no transition at each node are in parentheses and braces, respectively.

Figure Captions

Fig. 1 Layout of the self-organizing map, illustrating node selection and adaptation of neighboring nodes of a neural network to the input data.

Fig. 2 Spatial distribution of precipitation (mm/day) associated with self-organizing map classified patterns, obtained by compositing the Global Precipitation Climatology Project daily precipitation corresponding to the days clustered at the respective nodes. The arrows between figures illustrate evolutionary history of each node.

Fig. 3 Number of clustered days in each node for June–August. Base period is 30 years from 1979 to 2008. The arrows between figures illustrate evolutionary history of each node.

Fig. 4 First two leading eigenvectors obtained from empirical orthogonal function analysis of daily Global Precipitation Climatology Project precipitation data for June–August.

Fig. 5 Composite map of 500-hPa geopotential height (contour) and 850-hPa wind (vector) anomalies (only greater than 1.5 m/s) for (a) Meiyu–Baiu mode, (b) Changma mode, (c) post-Changma mode, and (d) dry-spell mode. 200-hPa zonal wind above 20 m/s is indicated by the shaded region.

Fig. 6 Composite map of simultaneous summertime (JJA) 850-hPa geopotential height (left) anomalies and preceding wintertime (DJF) SST (right) and for the years with high occurrence of the four modes. Critical positive (negative) values exceeding the 95% significance level are lightly (darkly) shaded.

Fig. 7 Lead–lag correlations among annual number of clustered days for the four major nodes and Niño-3 index.

Fig. 8 Mean annual number of days clustered at the four major nodes. The number of days clustered at each node for El Niño years (La Niña years) is described in dark (light) gray bars. The left (right) number on the upper left corner is an increased or decreased percentage of mean number of days for El Niño years (La Niña years) compare to total mean.

Table 1. Description of the six East Asian summer monsoon circulation indices. U is zonal wind, V is meridional wind, and Z is geopotential height.

Indices	Definition
CI500H	Z500 [25°N~35°N, 135°E~152.5°E]
CI850U	U850 [32.5°N~37.5°N, 127.5°E~147.5°E]
CI850V	V850 [32.5°N~37.5°N, 127.5°E~147.5°E]
RM2	U200 [40°N~50°N, 110°E~150°E] - U200 [25°N~35°N, 110°E~150°E]
SI	U850 [5°N~15°N, 90°E~130°E] - U200 [5°N~15°N, 90°E~130°E]
WNPMI	U850 [5°N~15°N, 100°E~130°E] - U850 [20°N~30°N, 110°E~140°E]

Table 2. Mean days per event, represented by bold type. Percent frequency of days and the probability of no transition at each node are in parentheses and braces, respectively.

(1,1) **6** (18.4%) {78.9}	(2,1) **3** (7.1%) {52.0}	(3,1) **4** (12.6%) {69.2}
(1,2) **3** (9.2%) {44.9}	(2,2) **2** (3.6%) {26.8}	(3,2) **3** (7.8%) {35.5}
(1,3) **4** (14.7%) {69.2}	(2,3) **3** (8.4%) {51.1}	(3,3) **5** (18.1%) {75.4}

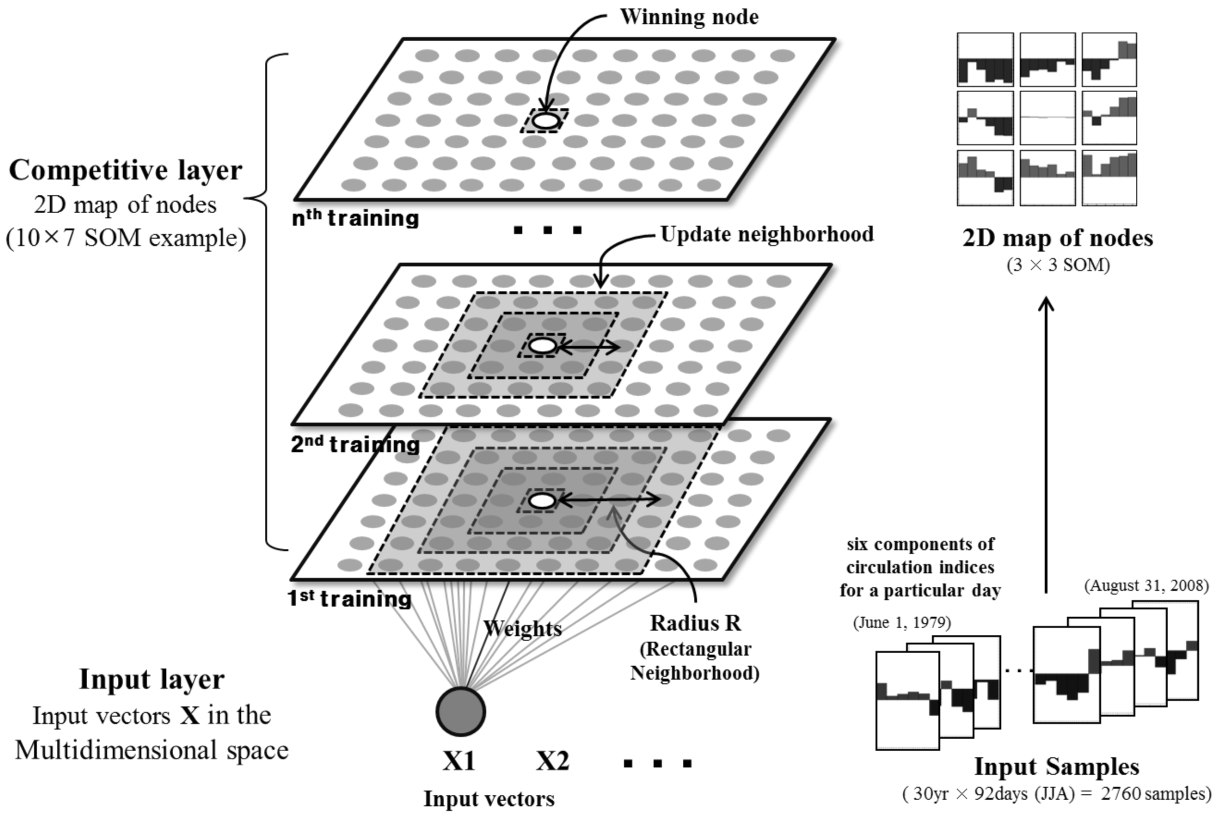

Fig. 1 Illustration of how SOM works in 2-dimensional (10×7) map of nodes (left side) and application of SOM with input data consisting of six monsoon circulation indices (right side).

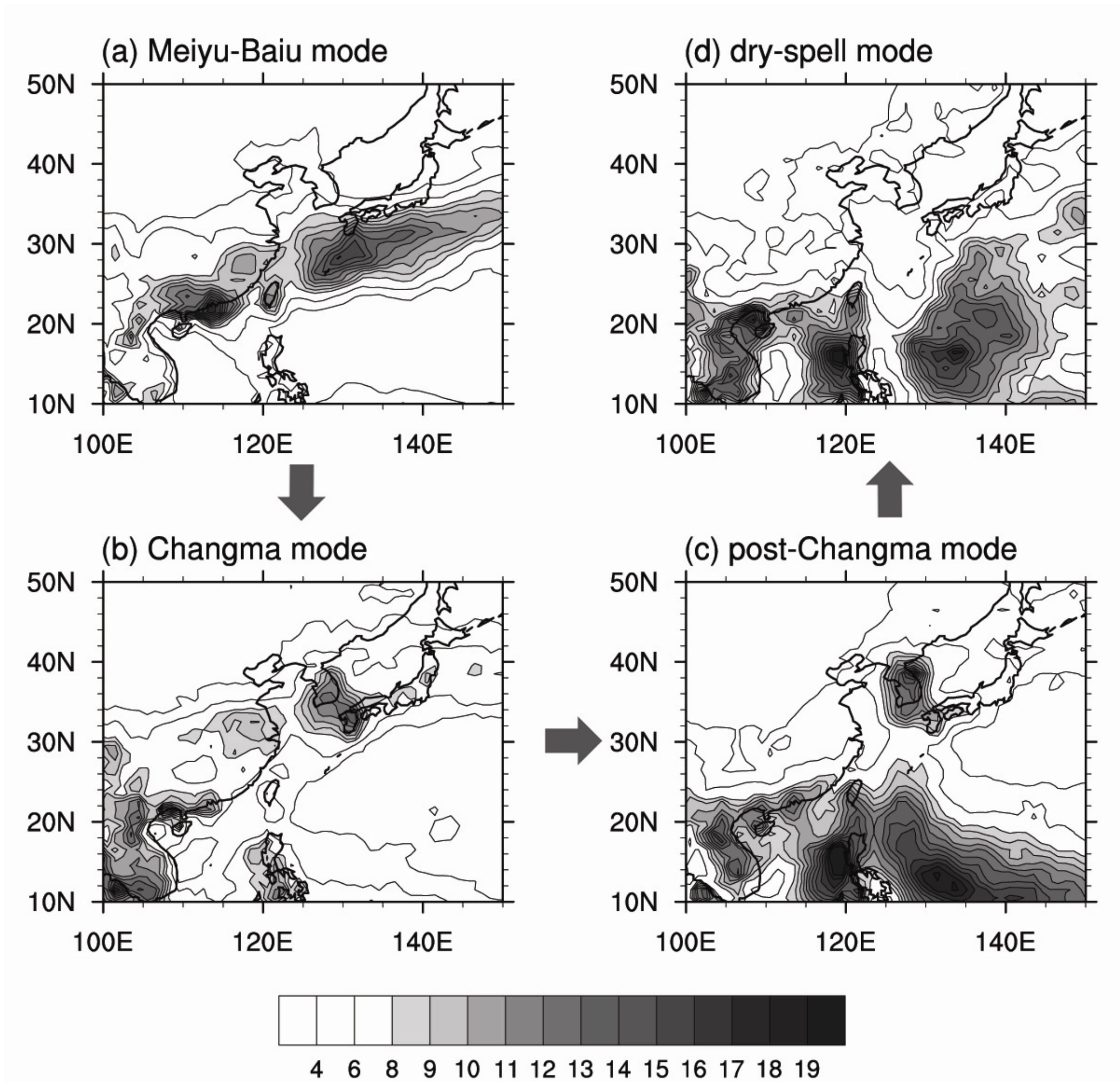

Fig. 2 Spatial distribution of precipitation (mm/day) associated with self-organizing map classified patterns, obtained by compositing the Global Precipitation Climatology Project daily precipitation corresponding to the days clustered at the respective nodes. The arrows between figures illustrate evolutionary history of each node.

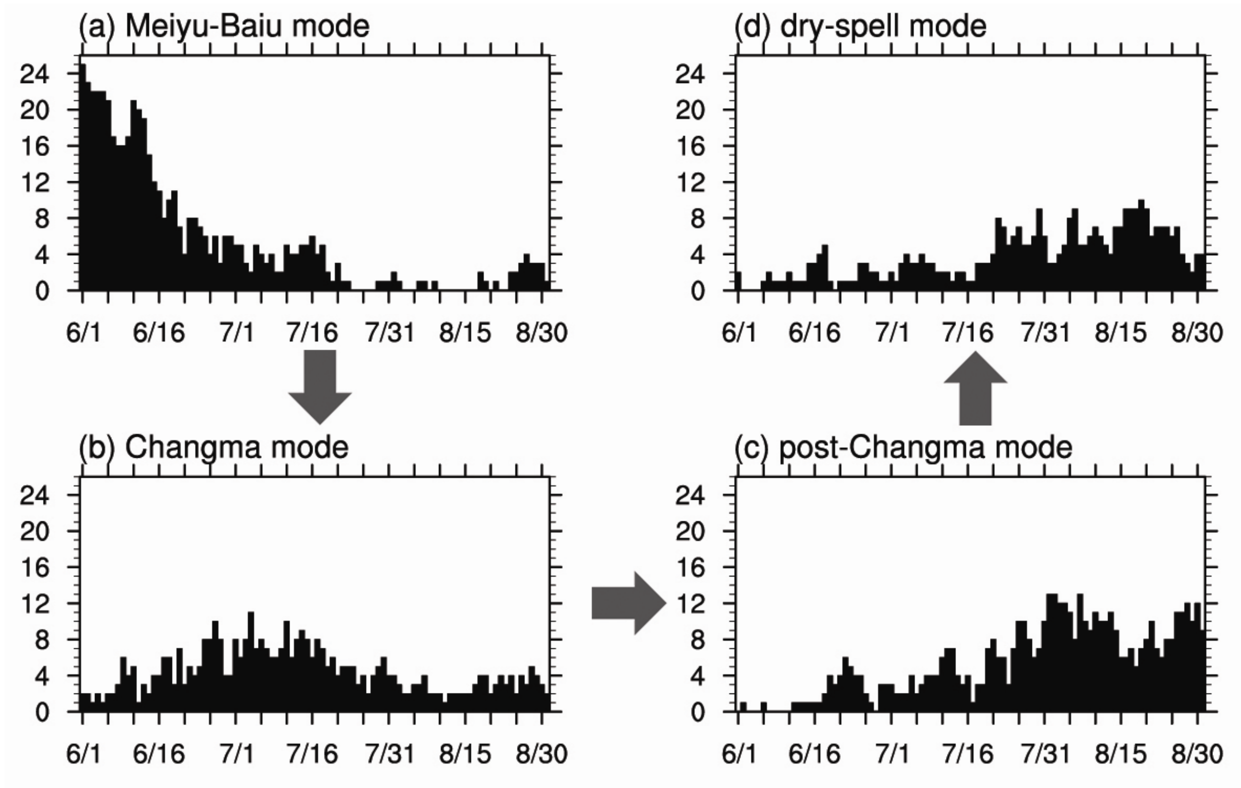

Fig. 3 Number of clustered days in each node for June–August. Base period is 30 years from 1979 to 2008. The arrows between figures illustrate evolutionary history of each node.

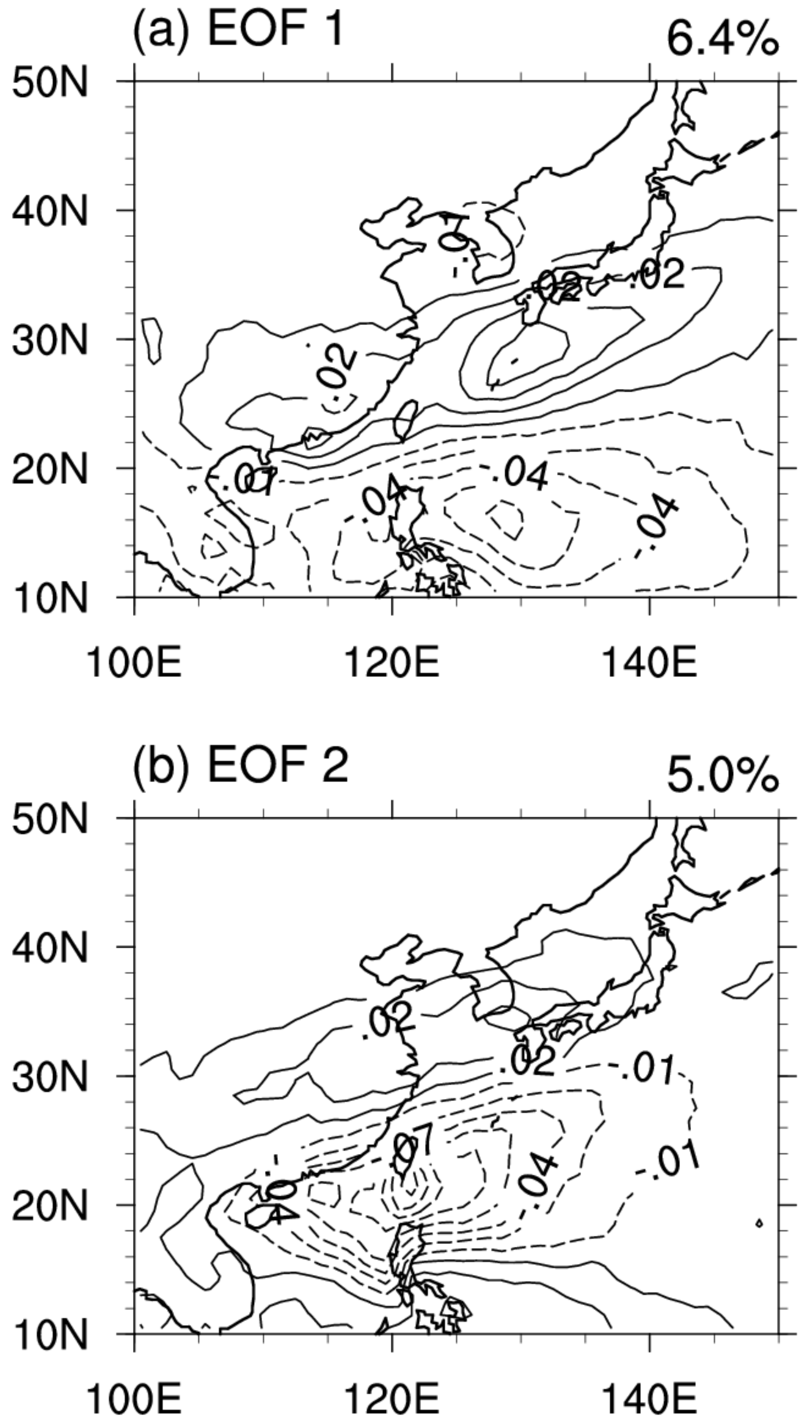

Fig. 4 First two leading eigenvectors obtained from empirical orthogonal function analysis of daily Global Precipitation Climatology Project precipitation data for June–August.

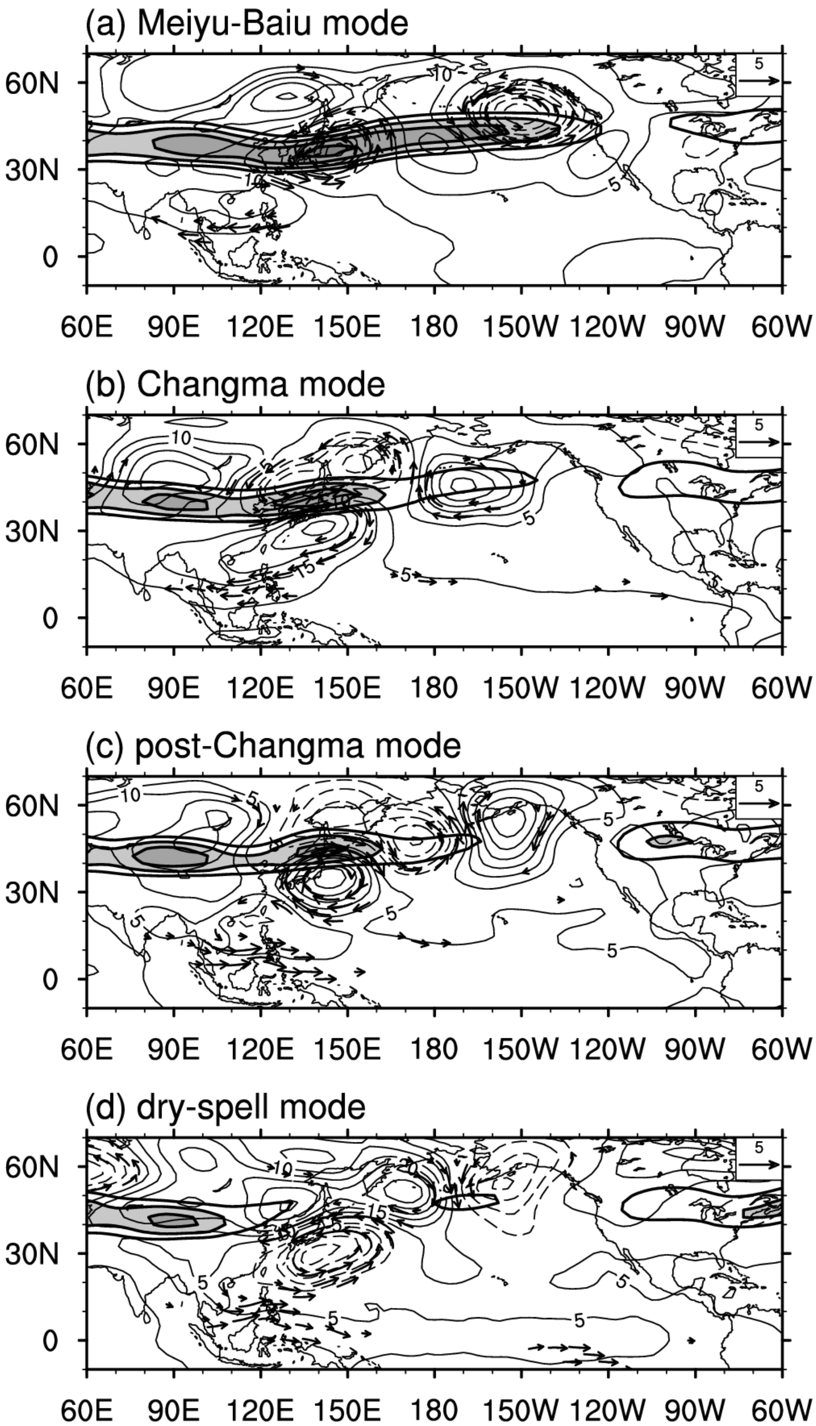

Fig. 5 Composite map of 500-hPa geopotential height (contour) and 850-hPa wind (vector) anomalies (only greater than 1.5 m/s) for (a) Meiyu-Baiu mode, (b) Changma mode, (c) post-Changma mode, and (d) dry-spell mode. 200-hPa zonal wind above 20 m/s is indicated by thick lines with 5 m/s contour intervals.

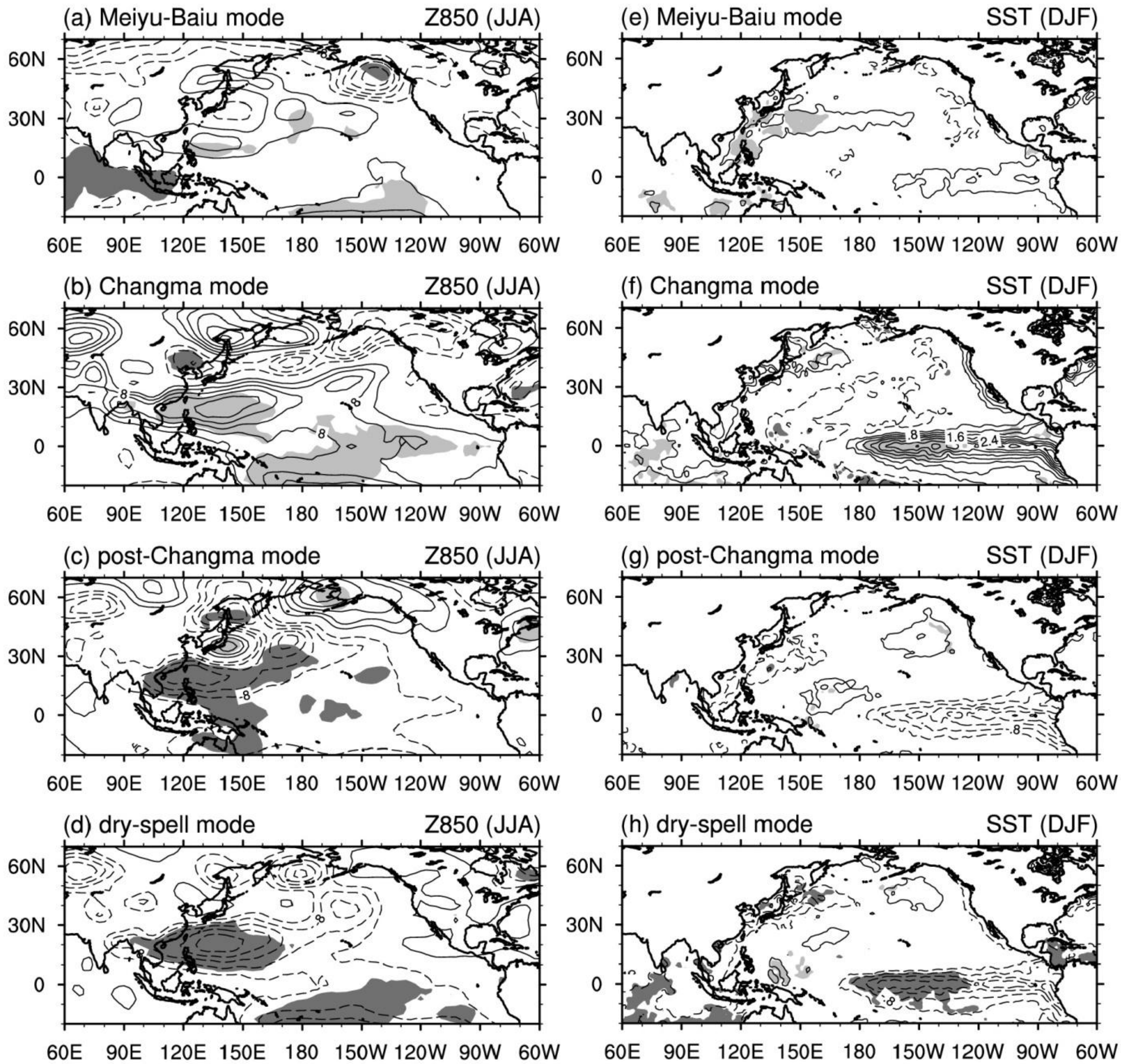

Fig. 6 Composite map of simultaneous summertime (JJA) 850-hPa geopotential height (left) anomalies and preceding wintertime (DJF) SST (right) and for the years with high occurrence of the four modes. Critical positive (negative) values exceeding the 95% significance level are lightly (darkly) shaded.

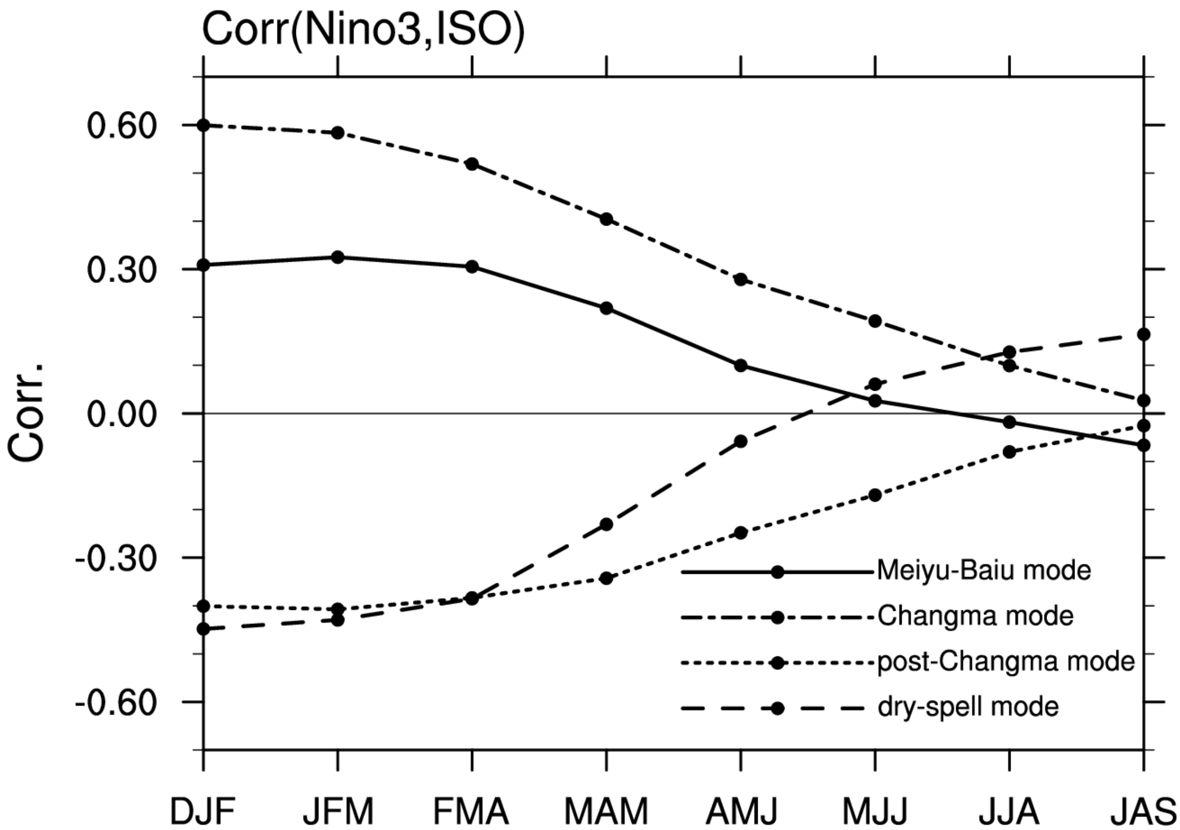

Fig. 7 Lead–lag correlations among annual number of clustered days for the four major nodes and Niño-3 index.

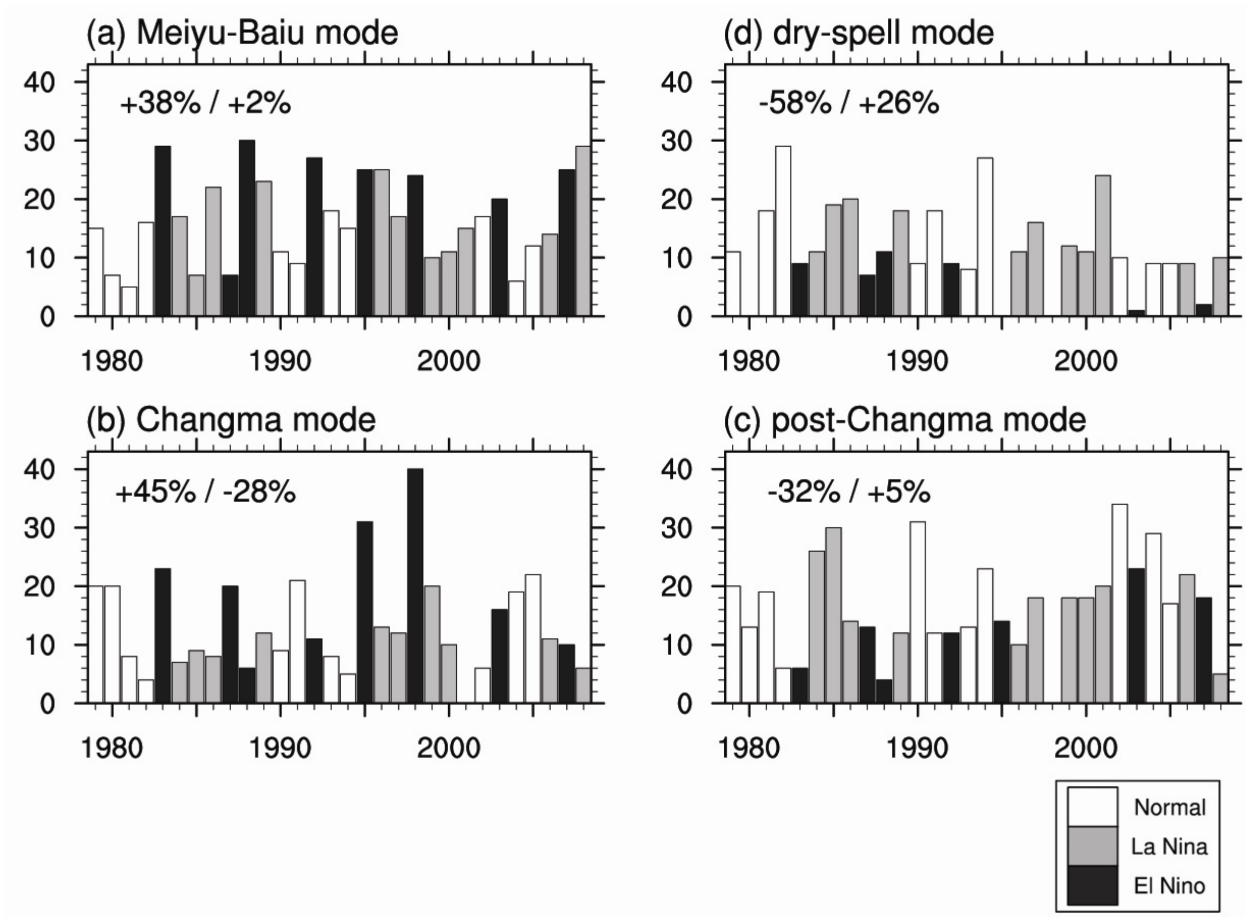

Fig. 8 Mean annual number of days clustered at the four major nodes. The number of days clustered at each node for El Niño years (La Niña years) is described in dark (light) gray bars. The left (right) number on the upper left corner is an increased or decreased percentage of mean number of days for El Niño years (La Niña years) compare to total mean.